ARCHIVES
of
FOUNDRY ENGINEERING

ISSN (2299-2944)

10.24425/afe.2026.158015

Published quarterly as the organ of the Foundry Commission of the Polish Academy of Sciences

Analysis of the Phase Composition and Microstructure of Slag from a Semi-Steel Converter

Li Chenxiao *, Wei Yongcong, Zhao Peng, Zhang Kaixuan, Gao Qianqian, Feng Zikang
College of Metallurgy and Energy, North China University of Science and Technology
Corresponding author: E-mail address: lichenxiao34@163.com

Received 22.05.2026; accepted in revised form 26.06.2026; available online 31.08.2026

Abstract

To clarify the phase composition, microstructural characteristics, and phosphorus retention mechanisms of semi-steel converter slag, this study employed characterization techniques such as XRD, SEM-EDS, FTIR, and Raman spectroscopy to systematically compare the mineral composition, phosphorus retention patterns, and microstructure of semi-steel converter slag with those of single-slag converter slag. The results show that the main mineral phases in both types of slag are C_2F, C_2S, and the RO phase; in single-slag converter slag, phosphorus primarily exists as n-dicalcium silicate-tricalcium phosphate solid solutions, with a small amount tending to be fixed in the glass phase and other phosphates; in semi-steel converter slag, phosphorus is enriched in the form of nC_2S-C_3P solid solutions and C_3P, with a small amount present in the glass phase and phosphorus-containing solid solutions; Both types of slag are composed of phosphates, silicates, and iron-aluminum coordination structures, with relatively low siloxane polymerization degrees, and P-O-P and P-O-Si are not major structural units. However, there are significant differences in the iron coordination environment: in semi-steel converter slag, iron primarily exists as FeO_4 tetrahedra and FeO_6 octahedra, whereas in single-slag converter slag, iron tends to form FeO_4 tetrahedra; furthermore, the silicon and phosphorus group content and network polymerization degree in single-slag converter slag are significantly higher than those in semi-steel converter slag. This study provides a theoretical basis for the resource utilization of converter slag and the optimization of smelting process parameters.

Keywords: Semi-steel converter slag, Single-slag converter slag, Phosphorus, Phase composition, Microstructure

1. Introduction

As a vital foundation of the national economy, the steel industry has long regarded efficiency, environmental sustainability, and sustainable development as the cornerstones of its research [1-2]. In recent years, international iron ore prices have risen annually. To reduce smelting costs, some enterprises have turned to domestically mined low-grade vanadium-titanium magnetite, which directly results in high levels of vanadium, titanium, and phosphorus in the molten iron. After vanadium extraction, this molten iron is referred to as “semi-steel.” The vanadium extraction process removes large amounts of elements such as silicon and manganese from the molten iron, making slag formation difficult and hindering phosphorus removal. Phosphorus, as a harmful impurity in molten iron, must be removed to ensure the low-temperature impact toughness and weldability of steel [3]. In contrast, the converter slag produced from semi-steel smelting exhibits significant differences in physicochemical properties compared to that from the single-slag method, presenting new challenges for the optimization of smelting processes and the efficient removal of phosphorus.

Converter slag is a direct product of the steelmaking process; its mineral composition and microstructure not only reflect the reaction mechanisms of the smelting process but also determine the metallurgical properties of the slag. Furthermore, the state of phosphorus in converter slag and its enrichment patterns are closely related to the efficiency of phosphorus removal and the subsequent resource utilization of the slag. Single-slag converter slag is a high-alkalinity steel slag, with a mineral composition primarily consisting of C_2S, C_3S, and RO phases (A continuous solid solution formed by divalent metal oxides such as FeO, MgO, and MnO), along with small amounts of free oxides, SiO_2, and metallic iron phases. Its microstructure is characterized by a multi-phase composite, and at the atomic scale, the melt structure varies with conditions such as alkalinity [4–5]. The mineral composition of semi-steel converter slag consists primarily of calcium-magnesium rhodochrosite, magnesium-iron phases, calcium-magnesium olivine phases, and small amounts of C_2S and C_3S. Its mineral morphology can be categorized into three main types: the gray phase is the silico-calcio-magnesian phase, the white phase is the magneferrous phase, and the grayish-white phase is the rhodochrosite phase or a composite phase of silicate and magneferrous phases. The phase composition and mineral morphology of semi-steel converter slag are influenced by alkalinity and cooling rate, which in turn affect its recovery and utilization. Semi-steel slag can be used for scrap steel recovery, road base materials, soil conditioners, and other applications [6]. Due to the high phosphorus content in the raw materials, the phase composition of semi-steel converter slag is more complex, and the crystallization habits, microstructures, and distribution patterns of the solid phosphorus-binding phases have undergone significant changes. A thorough analysis of these differences is crucial for understanding the limiting factors in phosphorus removal under semi-steel molten steel conditions.

Therefore, this study employed characterization techniques such as XRD, SEM-EDS, FTIR, and Raman spectroscopy to systematically compare the differences in mineral composition and microstructure between semi-steel converter slag and single-slag converter slag. It thoroughly elucidated the occurrence states and enrichment patterns of phosphorus in different slag systems, providing a theoretical foundation and scientific basis for the resource utilization of phosphorus in converter slag and the regulation of slag composition.

2. Test Samples and Testing Methods

2.1. Test samples

Two types of slag were selected: slag from the semi-steel converter at Hebei Chenggang Steel, designated as Type C slag; and slag from the single-slag method converter at Hebei Tanggang Steel, designated as Type T slag. The chemical compositions were analyzed using an X-ray fluorescence spectrometer. The results are shown in Table 1. The major elements in both types of slag were Ca, Fe, Si, Mg, P, Al, and Mn, with Type T slag exhibiting a slightly higher ternary alkalinity than Type C slag.

The melting points of the slags were determined using a ash melting point tester, and the results are shown in Table 2. As shown in Table 2, the melting point of Type C slag is slightly higher than that of Type T slag; consequently, Type C slag is more difficult to melt.

The viscosity of the two types of slag was calculated using the Factsage thermodynamic software. First, using the chemical compositions of the slags described above, the volume fractions of solids in the mixture were calculated in the Equilib module, and the composition of the liquid mixture was recorded. Next, using the composition of the liquid mixture, the viscosity of the liquid in the mixture was calculated in the Viscosity module. Finally, the viscosity of the liquid-solid mixture was calculated using the Einstein-Roscoe equation. The viscosities of the two types of slag are shown in Table 3. Table 3 shows that within a certain temperature range, as the temperature increases, the viscosity of both types of slag decreases and their fluidity gradually improves; under the same temperature conditions, Type C slag has lower viscosity.

A comparison of the physicochemical parameters of the two slags reveals that semi-steel converter slag exhibits characteristics of low alkalinity, high melting point, and low viscosity. The reasons for the low alkalinity, high melting point, and low viscosity of semi-steel converter slag are as follows: the semi-steel has a low carbon content and low silicon and manganese content; there is insufficient heat input in the early stages; the low-alkalinity acidic base slag itself has a high melting point; and the slag viscosity is forcibly reduced through intense oxygen supply and high-temperature smelting of the molten pool, resulting in a high-melting-point, thin slag.

Table 1.
Chemical composition of slag %

Sample Name	CaO	SiO_2	Fe_2O_3	Al_2O_3	P_2O_5	MgO	MnO	V_2O_5	Total alkalinity
Type C slag	35.80	6.51	30.50	2.37	5.01	7.90	0.82	1.27	3.11
Type T slag	43.60	10.60	24.60	0.96	2.08	3.59	1.87	0.28	3.43

Table 2.
Melting point of the slag °C

Sample Name	Deformation temperature	Softening temperature	Hemispheric temperature	Flow temperature
Type C slag	1325	1402	1403	1405
Type T slag	1334	1394	1395	1399

Table 3.
Comparison of Slag Viscosity Values at Different Temperatures Pa·s

Sample Name	1400 ℃	1450 ℃	1500 ℃	1550 ℃	1600 ℃
Type C slag	0.1145	0.0847	0.0589	0.0342	0.0283
Type T slag	0.1516	0.1168	0.0905	0.0666	0.0290

2.2. Testing Methods

To gain a comprehensive understanding of the mineral composition, phosphorus distribution patterns, and microstructural differences between semi-steel converter slag and single-slag converter slag,
systematic testing and analysis were conducted using the following four methods:

XRD: The mineral phases of the samples were analyzed using a D/Max 2500 PC X-ray diffractometer from Rigaku Corporation (Japan). The diffraction angle range was 2 θ = 10 ° to 90 °, with a step size of 0.02 °·s^{-1}. The obtained data were used to identify mineral phases using Jade 6.5 software.

SEM-EDS: Samples were prepared from lumpy converter slag through cold embedding, grinding, and polishing. Microscopic morphology was observed using a Phenom G6 series benchtop scanning electron microscope from FEI (USA), and micro-area elemental composition was analyzed using the integrated energy dispersive spectrometer (EDS) to comprehensively characterize the mineral phases and their composition in the slag.

FTIR: Approximately 2 mg of the experimental slag sample was mixed with 200 mg of spectroscopic-grade anhydrous KBr and pressed into a thin film. Molecular structure analysis was performed using a Bruker Vertex 70 series FTIR spectrometer (Germany). The infrared spectral measurement range was 400–4000 cm^{-1}, with a resolution of 0.4 cm^{-1}.

RAMAN: Select a block of slag with uniform texture and use a Thermo Fisher Scientific DXR series Raman spectrometer to detect molecular microstructural information. The laser wavelength is 532 nm, the scanning range is 200–4000 cm^{-1}, and the wavenumber resolution is 1 cm^{-1}.

3. Analysis of Experimental Results

3.1. Mineralogical Analysis of Slag

X-ray diffraction (XRD) was used to analyze Type C and Type T slags, respectively. The data obtained were processed using Jade 6.5 and Origin 9.0 software for mineralogical analysis and pattern plotting. The XRD analysis results for the two types of slag are shown in Figure 1. The mineral composition of Type C slag consists primarily of C_2F, C_2S, $Ca_3(PO_4)_2$, RO phase (e.g., MgO, FeO), TiO_2, NaF, and Fe. The NaF is mainly formed by the combination of fluorine and sodium elements introduced from the vanadium-titanium magnetite feedstock at high temperatures. The mineral composition of T-type slag consists primarily of C_2F, $Mg_2Si_2O_6$, C_2S, CaO-MnO solid solutions, $Ca_3(PO_4)_2$, and the RO phase (e.g., FeO). The main mineral phases in both types of slag are C_2F, C_2S, and the RO phase, with only trace amounts of phosphorus-bearing phases.

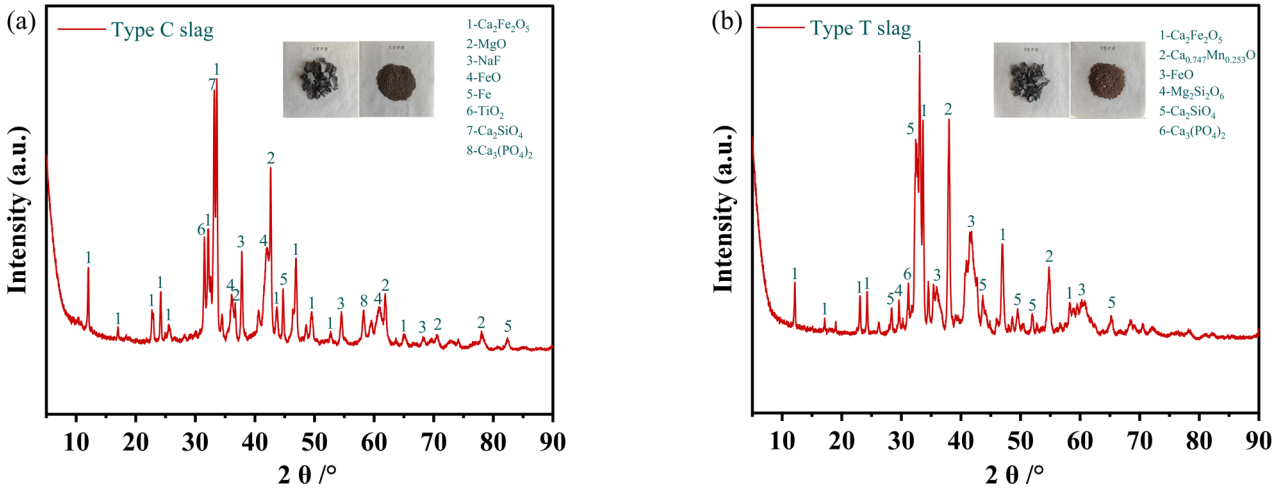

a) Type C slag b) Type T slag

Fig. 1. XRD diffraction pattern of the slag

3.2. A Study on the Distribution and Enrichment Patterns of Phosphorus in Micro-regions of Slag

To investigate the distribution and enrichment patterns of phosphorus in semi-steel converter slag and single-slag converter slag, SEM-EDS was used to characterize and analyze the two types of converter slag. The raw SEM morphologies of the two slags are shown in Figure 2. The Type C slag consists primarily of irregular block-like aggregates, whereas the gray phase in the Type T slag also contains leaf-like, spherical, and strip-like aggregates. Both slags consist of three color phases: black, gray, and white. To understand the elemental composition of the different phases, EDS point scanning analysis was performed, and the results are shown in Table 4. As shown in Figure 2 and Table 4, in the C-type slag, location I corresponds to the gray phase, with an Mg:Fe atomic ratio of approximately 3:1. This phase is dominated by MgO with FeO in solid solution and belongs to the magnesium-rich magnetite; location II corresponds to the white phase, which is high in Fe and Ca, rich in O, and poor in Si and Mg. with an Fe content of nearly 50 %, and is classified as a calcium ferrite phase; location III is a black phase with high Fe, Ca, and Mn contents, indicating a calcium-iron-manganese phosphate solid solution. This phase exhibits a dicalcium silicate morphology and is classified as dicalcium silicate, representing a phosphorus-rich phase; location IV is a gray phase, which is the most abundant phase in the steel slag, with a Ca content of 47.25 %, indicating a calcium phosphate matrix. It also exhibits the morphology of dicalcium silicate and is classified as dicalcium silicate, representing a phosphorus-rich phase. In T-type slag, location I consists of a banded-gray phase with an atomic Ca:Si ratio of approximately 5.2:1. It is a silicate phase exhibiting the morphology of tricalcium silicate and belongs to a composite of dicalcium silicate, tricalcium silicate, and free calcium oxide, classified as a phosphorus-rich phase; location II consists of a white phase that is high in iron, calcium, and manganese, with extremely low silicon and aluminum content; it is a solid solution of calcium-iron-manganese oxides and belongs to the calcium ferrite phase; Area III consists of a leaf-like, round-grained gray phase with a calcium-to-silicon ratio of approximately 3.2:1; it is a solid solution of silicates and phosphates, exhibiting the morphology of dicalcium silicate, and belongs to a composite of dicalcium silicate and free calcium oxide, constituting a phosphorus-rich phase; Location IV consists of a clumpy, gray phase with high calcium and low silicon and aluminum content; this is likely a free calcium oxide phase; Location V consists of a black phase with an atomic Mg:Fe ratio of approximately 4:1 and an atomic O:(Mg+Fe) ratio close to 1:1, indicating that this is a solid solution of periclase and magnetite, classified as magnesite-magnetite.

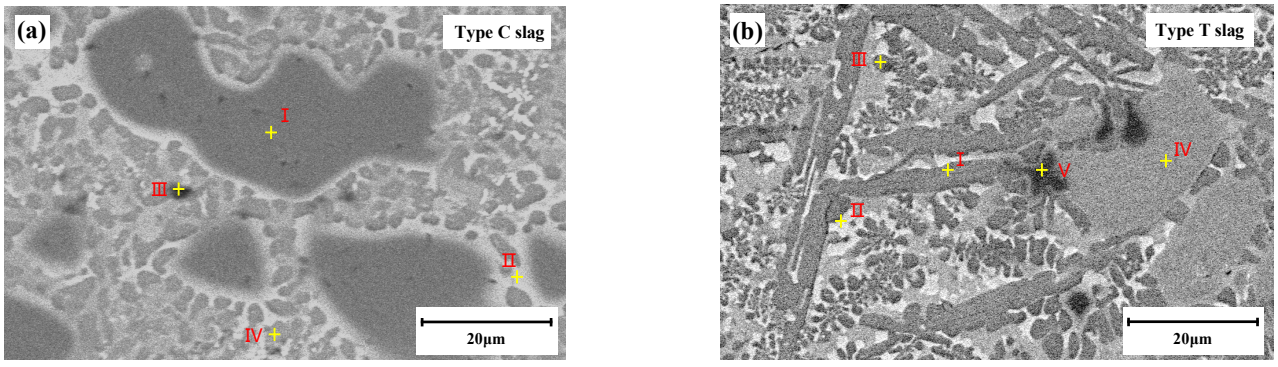

a) Type C slag b) Type T slag

Fig. 2. Original SEM image of the slag

Table 4.
EDS spot scan results for different phases %

Select scan location	Chemical Composition									
	Fe	Ca	O	Mg	Al	P	Si	Mn	V	Ti
C-I	16.70	1.50	35.80	42.50	0.30	0.40	-	1.80	0.70	0.30
C-II	46.35	13.41	28.63	6.11	0.40	0.40	0.50	3.00	0.30	0.90
C-III	25.33	19.72	30.53	3.00	3.20	3.60	3.70	8.61	1.00	1.30
C-IV	15.12	47.25	27.03	0.20	1.20	3.00	4.20	1.30	0.30	0.40
T-I	2.10	47.70	37.40	0.30	0.20	1.10	9.20	1.40	0.20	0.40
T-II	47.50	12.70	28.20	3.50	0.50	1.00	0.50	4.10	1.00	1.00
T-III	2.80	43.86	37.86	0.50	0.80	2.80	9.60	0.40	0.70	0.70
T-IV	3.10	55.16	35.14	2.60	0.20	0.80	0.30	2.70	-	-
T-V	14.80	1.90	36.50	41.40	0.10	0.50	-	3.50	0.70	0.60

To gain a more intuitive understanding of the distribution patterns of different elements, a surface scan analysis was performed on the original morphological images. The surface scan results for the slag are shown in Figure 3. Some elements in the slag exhibit distinct contours, and the distribution regions of Ca, P, and Si show a high degree of overlap. Phosphorus exists in the slag as a C_2S–C_3P solid solution and exhibits distinct distribution characteristics. Areas with high oxygen (O) brightness overlap with the distribution regions of Fe, Mg, and Mn, indicating that elements such as Mn and Mg, which were oxidized in the molten iron, have all entered the matrix phase. Phosphorus is highly concentrated in the calcium-rich phase, and the RO phase shows virtually no solid solution with phosphorus. In Type T slag, there is a phenomenon of reduced phosphorus aggregation. The low phosphorus content leads to a decrease in surface sweep counts, which in turn results in the observed reduction in aggregation. However, the form in which phosphorus is immobilized in Type T slag remains unchanged; phosphorus primarily exists as an nC_2S-C_3P solid solution.

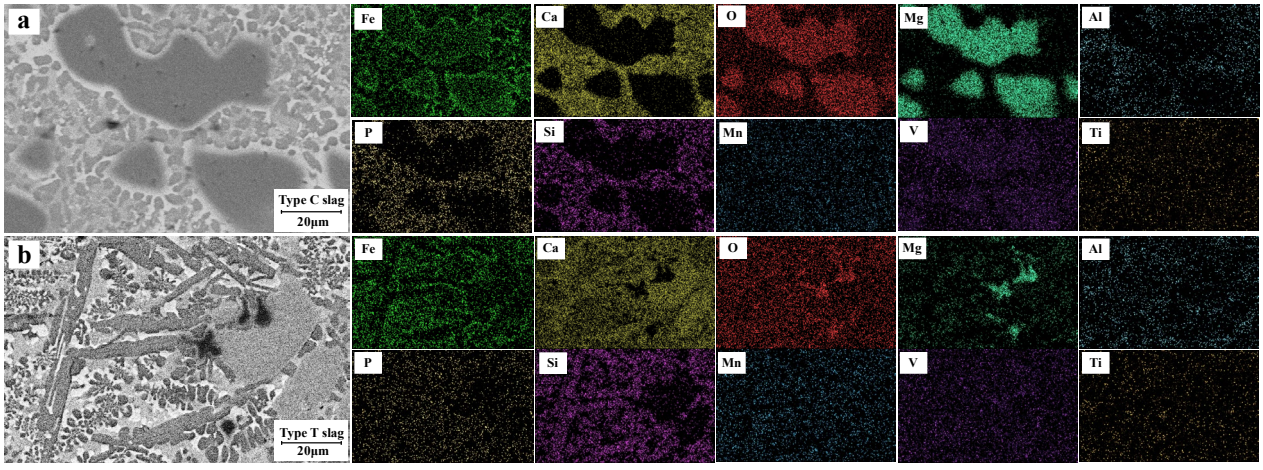

a) Type C slag b) Type T slag

Fig. 3. SEM images of the original slag morphology

A comprehensive study of the two types of slag using SEM-EDS characterization revealed that in semi-steel slag, the initial phosphorus content is relatively high and its distribution is relatively concentrated. During the enrichment process, phosphorus first combines with Ca^{2+} in the form of PO_4^{3-} to form stable C_3P. C_2S, which acts as a phosphorus carrier, combines with C_3P to form an nC_2S-C_3P solid solution. In contrast, the semi-steel melt contains relatively low levels of elements such as Si and Mn. During the reaction, a small amount of phosphorus rapidly consumes the Si, forming a stable nC_2S-C_3P solid solution, while unbound phosphorus exists as C_3P. Therefore, phosphorus is primarily concentrated in the slag as nC_2S-C_3P solid solutions and C_3P, with a small amount present in the glass phase and phosphorus-containing solid solutions. In single-slag converter slag, due to the low total phosphorus content, phosphorus is distributed more diffusely within the slag. Phosphorus primarily exists as an nC_2S-C_3P solid solution, with a small amount tending to be fixed in the glass phase and other phosphates.

3.3. Comparative Analysis of the Microstructure of Slag

To analyze the microstructural differences between the two types of slag, complementary analyses using infrared spectroscopy and Raman spectroscopy were conducted; infrared spectroscopy is more sensitive to asymmetric structures, while Raman spectroscopy is more sensitive to symmetric structures. First, infrared spectroscopy was performed on Type C and Type T slags, with two sets of tests conducted for each type. By comparing multiple data sets, measurement system errors were effectively eliminated. The results are shown in Figure 4. The infrared absorption peaks at 500–600 cm^{-1} correspond to the symmetric stretching vibrations of the P=O and the P–O bond in the $[PO_4]^-$ group [7], indicating the presence of PO_4^{3-}. Among these, the C-2 vibrational peak in Type C slag is the weakest, suggesting the lowest PO_4^{3-} content in Type C slag at this wavelength, while the T-2 vibrational peak in Type T slag is the strongest, indicating the highest PO_4^{3-} content in Type T slag. The region near 700 cm^{-1} corresponds to FeO_4 vibrations [8] and P-O-P bonds [9], reflecting the presence of tetrahedral iron structures and phosphorus-oxygen networks. The T-2 vibrational peak is strongest in this region, indicating that T-type slag has the highest proportion of P-O-P and $[FeO_4]^{5-}$ structures at this location. The 800–1100 cm^{-1} region corresponds to the stretching vibrations of $[PO_4]^-$ and $[SiO4]^-$ [10], including the Q^0(Si), Q^1(Si), Q^2(Si), and Q^1(P) units. The intensity of the infrared absorption peaks in Type T slag is significantly higher than that in Type C slag, indicating that Type T slag has a higher content of silicon and phosphorus groups and a higher degree of network aggregation.

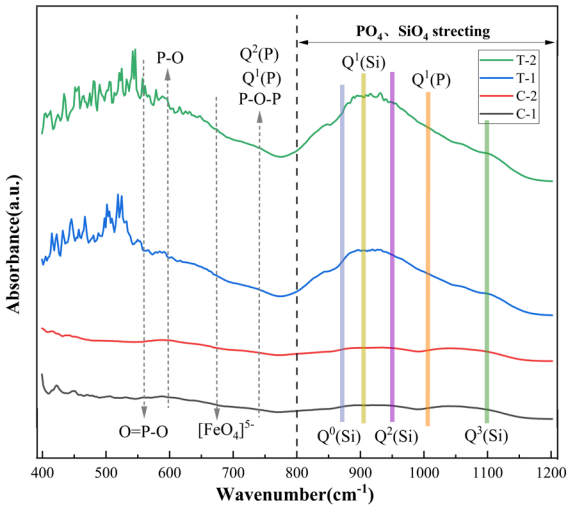

Fig. 4. Infrared spectrum of the slag

To further analyze the microstructural differences between the two types of slag, a Raman spectrometer was used to examine them. Two sets of tests were conducted for each type of slag (Type C and Type T). By comparing multiple sets of data, measurement system errors could be effectively eliminated. The Raman spectra of the two types of slag are shown in Figure 5. The region between 580 and 700 cm^{-1} corresponds to the Fe-O stretching vibration [11–13], which is associated with the FeO_4 tetrahedral and FeO_6 octahedral structures. The peak in the C-type slag spectrum is broad and distinct, indicating that Fe in C-type slag is primarily coordinated in an octahedral configuration. In contrast, the peak in the T-type slag spectrum is weaker, suggesting that Fe in T-type slag may occupy tetrahedral sites. Both types of slag exhibit distinct peak positions, but there is overlap in the complexation peaks, requiring de-convolution processing. The region at 640–660 cm^{-1} corresponds to the Al–O stretching vibration [14–15], which is associated with the AlO_4 tetrahedral structure. Type C slag exhibits a peak at this position, while Type T slag shows no distinct peak, suggesting that the Al–O bond is not a primary structural feature here. The increasing peak intensity in both slags is related to the [FeOx] structure. The region at 740–800 cm^{-1} corresponds to the P-O-P symmetric stretching [16–19]. The peak shapes of the curves for both types of slag are flat, indicating that this is not a major structural bond. In the 800–1050 cm^{-1} region, there are bond shifts such as Q^0(Si), Q^1(Si), Q^2(Si), Q^0(P), and Q^1(P) [20–25]. The peak intensities for both types of slag are relatively weak, indicating that silicate tetrahedra exist at different degrees of polymerization, with a lower degree of polymerization. The 1050–1152 cm^{-1} region corresponds to P-O-Si stretching vibrations and Q^2(P) bond shifts [5]. Type C slag exhibits distinct vibrational peaks, indicating the presence of phosphate and silicate structures, whereas Type T slag shows weak peaks in this region, suggesting that the vibrational signals from phosphate structures are faint.

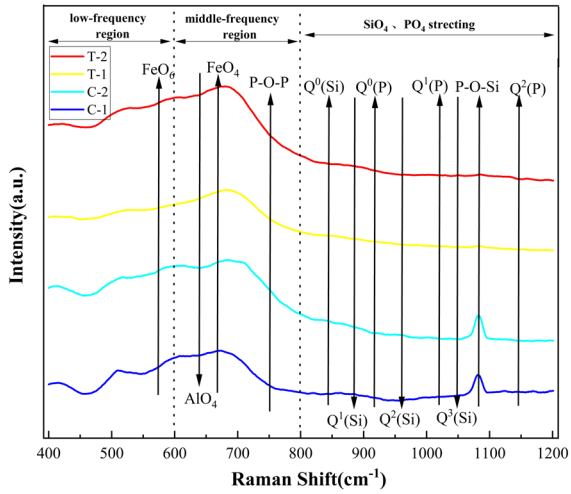

Fig. 5. Raman spectrum of the slag

Due to the overlap of the vibrational peaks of phosphates, silicates, and ferrites, as well as the overlap of numerous complexation peaks across the entire spectral range, deconvolution is required to better distinguish the variations in each vibrational peak. The deconvolution was performed using Origin 9.0 software. First, the raw curves were smoothed, followed by baseline flattening. Subsequently, Gaussian deconvolution was applied to perform peak-by-peak fitting until the minimum correlation coefficient R^2 exceeded 0.99. Numerous researchers have employed this method for deconvolution, demonstrating its accuracy and feasibility [26].

The Raman spectra of Type C and Type T slags were deconvoluted separately. The deconvoluted results for the two slags are shown in Figure 6. The Type C slag primarily exhibits five vibrational peaks: FeO_4 tetrahedral vibration, FeO_6 octahedral stretching vibration, Si-O-Si bending vibration, Q^0(Si), and P-O-P vibration. In Type T slag, the five main vibrational peaks are those of the FeO^4 tetrahedral structure, Si-O stretching, Q^1(Si), Q^2(P), and P-O-Si asymmetric stretching. In both types of slag, silicates primarily exist in the form of low-polymerization silicates such as Q^0(Si) and Q^1(Si). At the same time, the vibrational peak areas of the FeO_4 tetrahedron and FeO_6 octahedron account for the largest proportion, indicating that they are the most abundant in the slag; P-O-P and P-O-Si are not major structural units, indicating that the slag contains only trace amounts of phosphorus-containing phases, a result that is consistent with the XRD findings.

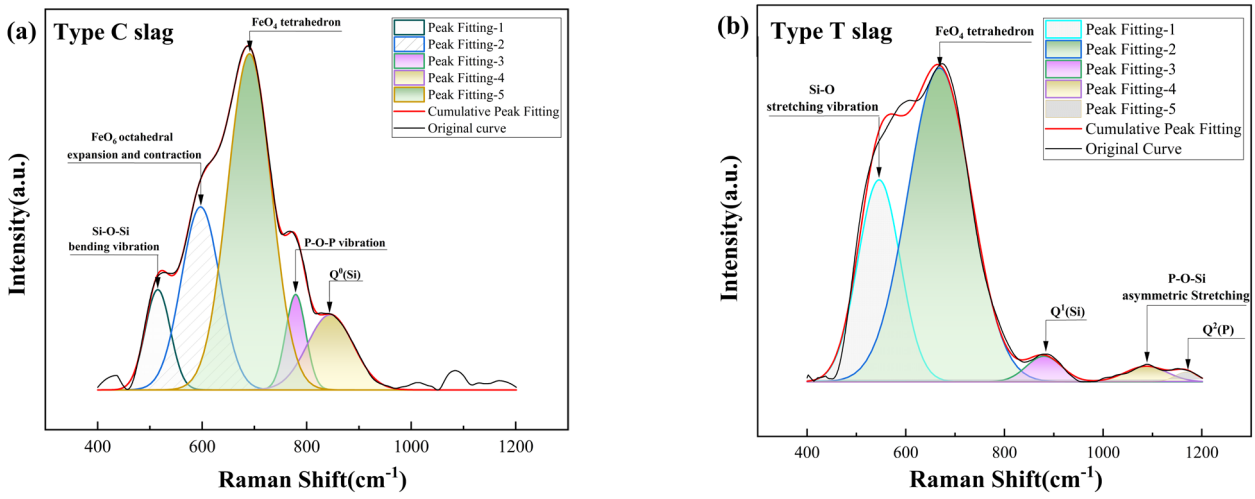

a) Type C slag b) Type T slag

Fig. 6. Deconvolution results of the Raman spectrum of the slag

A comparison of the microstructures of the two slags using FTIR and Raman spectroscopy revealed that both slag systems exhibit coordination structures and network bonding characteristics centered on PO_4^{3-}, SiO_4^{4-}, Fe-O, and Al-O. Both slags are composed of phosphate, silicate, and iron-aluminum coordination structures, and the degree of siloxane polymerization in the slags is generally low. and P-O-P and P-O-Si bonds are not the primary structural units. There are significant differences in the coordination environment of iron between the two slags. In semi-steel converter slag, iron primarily exists in the form of FeO_4 tetrahedra and FeO_6 octahedra, whereas in single-slag converter slag, iron tends to adopt FeO_4 tetrahedral coordination. Notably, the silicon and phosphorus group content, as well as the degree of network polymerization, in single-slag converter slag are significantly higher than those in semi-steel converter slag.

4. Conclusions

1) The main mineral phases in semi-steel converter slag are C_2F, C_2S, $Ca_3(PO_4)_2$, the RO phase, TiO_2, and NaF, among others. The main mineral phases in single-slag converter slag are C_2F, $Mg_2Si_2O_6$, C_2S, CaO-MnO solid solutions, $Ca_3(PO_4)_2$, and the RO phase.
2) In semi-steel slag, phosphorus is primarily concentrated in the slag in the form of nC_2S-C_3P solid solutions and C_3P; a small amount of phosphorus is present in the glass phase and phosphorus-containing solid solutions. In single-slag converter slag, phosphorus exists mainly in the form of nC_2S-C_3P solid solutions, with a small amount tending to be fixed in the glass phase and other phosphates.
3) Both types of slag consist of phosphate, silicate, and iron-aluminum coordination structures; the degree of siloxane polymerization is relatively low in both cases, and P-O-P and P-O-Si are not the primary structural units. However, there are significant differences in the coordination environment of iron: in semi-steel converter slag, iron primarily exists in FeO_4 tetrahedra and FeO_6 octahedra, whereas in single-slag converter slag, iron tends to form FeO_4 tetrahedra. In contrast, due to its higher alkalinity and SiO_2 content, single-slag converter slag has higher silicon and phosphorus group content and a higher degree of network polymerization than semi-steel converter slag.

Acknowledgements

This work was supported by the Hebei Province Innovation Ability Improvement Plan (Project No. 26361004D) and the Hebei Provincial Natural Science Foundation (Project No. E2026209004).

References

[1] Chen, K., Wang, D. & Guo, A. (2025). Research on green development efficiency of iron and steel industry based on super-efficient SBM-malmquist index modeling. *International Core Journal of Engineering*. 11(6), 23-32. https://doi.org/10.6919/ICJE.202506_11(6).0003 .
[2] Kasraee, A.R., Shirazi, H. & Alba, K.A. (2026). Scientometric review of green technologies in the steel industry. *Iranica Journal of Energy & Environment*. 17(1), 72-92. https://doi.org/10.5829/ijee.2026.17.01.07.
[3] Han, D.W., Qiu. J., Hu, F.W. et al. (2019). High efficiency dephosphorization method and low cost control for 150 t converter of bearing steel. China Metallurgical Society. In Proceedings of the 12th China Iron and Steel Annual Conference—Vol. 2: Steelmaking and Continuous Casting (pp. 500-505). Beijing: Metallurgical Industry Press.
[4] Zhang, Z. L., Chen, R., Men, X. R. & Sun, Y. (2019). Phase compositions and microstructure of slag in BOF. *Journal of Materials and Metallurgy*. 18(1), 37-40.
[5] Zhang, R., Jia, J.X., Liu, C. & Min, Y. (2021). Microstructure behaviors of phosphorus in converter slag.

Journal of Northeastern University (Natural Science). 42(5), 646-651.

[6] Liang, X.L., Wang, X.H., He, X.F. & Wang, W.J. (2014). Mineral phase and utilization of semisteel slag produced during BOF double slag process. *Journal of Iron and Steel Research*. 26(10), 15-20.

[7] Zhou, C., Chen, Q., Zhao, J., Ai, L., Wang, S., Shi, D. & Li, J. (2023). Effect of sinter return ore addition on dephosphorisation behaviour of hot metal. *ISIJ International*. 63(11), 1842-1853. https://doi.org/10.2355/isijinternational.ISIJINT-2023-183.

[8] Agathopoulos, S., Tulyaganov, D.U., Ventura, J.M.G., Kannan, S., Saranti, A., Karakassides, M.A. & Ferreira, J.M. F. (2006). Structural analysis and devitrification of glasses based on the CaO–MgO–SiO_2 system with B_2O_3, Na_2O, CaF_2 and P_2O_5 additives. *Journal of Non-Crystalline Solids*. 352(4), 322-328. DOI: 10.1016/j.jnoncrysol.2005.12.003.

[9] Li, B. & Zhou, G. (2025). Preparation of phosphate glass by the conventional and microwave melt-quenching methods and research on its performance. *Materials*. 18(5), 1079, 1-20. https://doi.org/10.3390/ma18051079.

[10] Sun, Y., Zhang, Z., Liu, L. & Wang, X. (2015). FTIR, Raman and NMR investigation of CaO–SiO_2–P_2O_5 and CaO–SiO_2–TiO_2–P_2O_5 glasses. *Journal of Non-Crystalline Solids*. 420, 26-33. DOI: 10.1016/j.jnoncrysol.2015.04.017.

[11] Wang, Z., Sun, Y., Sridhar, S., Zhang, M., Guo, M. & Zhang, Z. (2015). Effect of Al_2O_3 on the viscosity and structure of CaO–SiO_2–MgO–Al_2O_3–FetO slags. *Metallurgical and Materials Transactions B*. 46(2), 537-541. https://doi.org/10.1007/s11663-015-0303-4.

[12] Lucazeau, G., Sergent, N., Pagnier, T., Shaula, A., Kharton, V. & Marques, F. M. B. (2007). Raman spectra of apatites: $La_{10-x}Si_{6-r}(Al, Fe)_rO_{26\pm\delta}$. *Journal of Raman Spectroscopy*. 38(1), 21-33. https://doi.org/10.1002/jrs.1569.

[13] Zhang, R., Wang, Y., Zhao, X., Jia, J., Liu, C. & Min, Y. (2020). Structure and viscosity of molten CaO–SiO_2–Fe_xO slag during the early period of basic oxygen steelmaking. *Metallurgical and Materials Transactions B*. 51(5), 2021-2029. https://doi.org/10.1007/s11663-020-01888-8.

[14] Jung, S. S. & Sohn, I. (2014). Crystallization control for remediation of an Fe_tO-rich CaO–SiO_2–Al_2O_3–MgO EAF waste slag. *Environmental Science & Technology*. 48(3), 1886-1892.

[15] Li, T., Zhao, C., Sun, C., Song, S., & Wang, Q. (2020). Roles of MgO and Al_2O_3 in viscous and structural behavior of blast furnace primary slag with C/S=1.4. *Metallurgical and Materials Transactions B*. 51(6), 2724-2734. https://doi.org/10.1007/s11663-020-01980-z.

[16] Duan, R.G., Liang, K.M. & Gu, S.R. (1998). Effect of Na^+ ion on the structure of $27CaO{\cdot}12Al_2O_3{\cdot}61SiO_2$ glass. *Materials Chemistry and Physics*. 57(1), 92-94. https://doi.org/10.1016/S0254-0584(98)00207-7.

[17] Stoch, P., Goj, P., Ciecińska, M., Jeleń, P., Błachowski, A., Stoch, A. & Krakowiak, I. (2020). Influence of aluminum on structural properties of iron–polyphosphate glasses. *Ceramics International*. 46(11), 19146-19157. https://doi.org/10.1016/j.ceramint.2020.04.250.

[18] Stoch, P., Stoch, A., Ciecinska, M., Krakowiak, I. & Sitarz, M. (2016). Structure of phosphate and iron–phosphate glasses by DFT calculations and FTIR/Raman spectroscopy. *Journal of Non-Crystalline Solids*. 450: 48-60. DOI: 10.1016/j.jnoncrysol.2016.07.027.

[19] Goj, P., Wajda, A. & Stoch, P. (2021). Raman imaging as a useful tool to describe crystallization of aluminum/iron-containing polyphosphate glasses. *Journal of the European Ceramic Society*. 41(8), 4572-4583. https://doi.org/10.1016/j.jeurceramsoc.2021.03.028.

[20] Sun, Y. & Zhang, Z. (2015). Structural roles of boron and silicon in the CaO–SiO_2–B_2O_3 glasses using FTIR, Raman, and NMR spectroscopy. *Metallurgical and Materials Transactions B*. 46(4), 1549-1554. https://doi.org/10.1007/s11663-015-0374-2.

[21] Park, Y. & Min, D.J. (2017). A structural study on the foaming behavior of CaO–SiO_2–Mo (Mo = MgO, FeO, or Al_2O_3) ternary slag system. *Metallurgical and Materials Transactions B*. 48(6), 3038-3046. https://doi.org/10.1007/s11663-017-1079-5.

[22] Wu, T., Zhang, Y., Yuan, F. & An, Z. (2018). Effects of the Cr_2O_3 content on the viscosity of CaO–SiO_2–10 pct Al_2O_3–Cr_2O_3 quaternary slag. *Metallurgical and Materials Transactions B*. 49(4), 1719-1731. https://doi.org/10.1007/s11663-018-1258-z.

[23] Fowler, B.O., Markovic, M. & Brown, W.E. (1993). Octacalcium phosphate. 3. Infrared and Raman vibrational spectra. *Chemistry of Materials*. 5(10), 1417-1423.

[24] Ding, J., Chen, Y., Chen, W., Hu, L. & Boulon, G. (2012). Effect of P_2O_5 addition on the structural and spectroscopic properties of sodium aluminosilicate glass. *Chinese Optics Letters*. 10(7), 071602-071602.

[25] Silva, A.M.B., Correia, R.N., Oliveira, J.M.M. & Fernandes, M. H. V. (2010). Structural characterization of TiO_2–P_2O_5–CaO glasses by spectroscopy. *Journal of the European Ceramic Society*. 30(6), 1253-1258. https://doi.org/10.1016/j.jeurceramsoc.2009.11.001.

[26] Zhang, R., Min, Y., Wang, Y., Zhao, X. & Liu, C. (2020). Structural evolution of molten slag during the early stage of basic oxygen steelmaking. *ISIJ International*. 60(2), 212-219. https://doi.org/10.2355/isijinternational.ISIJINT-2019-413.